CONDENSED MATTER PHYSICS

# Noninvasive measurements of spin transport properties of an antiferromagnetic insulator

**Hailong Wang[1], Shu Zhang[2], Nathan J. McLaughlin[3], Benedetta Flebus[4,5], Mengqi Huang[3], Yuxuan Xiao[1], Chuanpu Liu[6], Mingzhong Wu[6], Eric E. Fullerton[1], Yaroslav Tserkovnyak[2], Chunhui Rita Du[1,3]***



**Antiferromagnetic insulators (AFIs) are of substantial interest because of their potential in the development of next-generation spintronic devices. One major effort in this emerging field is to harness AFIs for long-range spin information communication and storage. Here, we report a noninvasive method to optically access the intrinsic spin transport properties of an archetypical AFI $\alpha$-$Fe_2O_3$ via nitrogen-vacancy (NV) quantum spin sensors. By NV relaxometry measurements, we successfully detect the frequency-dependent dynamic fluctuations of the spin density of $\alpha$-$Fe_2O_3$ along the Néel order parameter, from which an intrinsic spin diffusion constant of $\alpha$-$Fe_2O_3$ is experimentally measured in the absence of external spin biases. Our results highlight the significant opportunity offered by NV centers in diagnosing the underlying spin transport properties in a broad range of high-frequency magnetic materials such as two-dimensional magnets, spin liquids, and magnetic Weyl semimetals, which are challenging to access by the conventional measurement techniques.**

## INTRODUCTION

Advanced materials are integral to both scientific research and modern technology, enabling a wide range of emerging applications. Antiferromagnetic (AF) insulators (AFIs), a group of scientifically intriguing and technologically relevant materials, promise to bring new functionalities, such as high-density magnetic memory, ultrafast data processing speeds, and robust strategies, against malignant perturbations to develop transformative spin-based information technologies (*1*–*3*). Many of these advantages derive from their exchange-enhanced magnon bandgaps reaching into a terahertz regime and the vanishing net magnetization of the Néel order, which enable opportunities for outperforming their ferromagnetic counterparts (*4*–*8*).

Recent efforts have pursued effective control and manipulation of the Néel orientation in a range of AFIs (*9*–*14*). Building on the excellent spin coherence and reduced energy dissipation channels, AFIs naturally stand out as an attractive solid-state medium to support long-range, energy-efficient transmission of spin information (*15*–*17*). In the present state of the art, spin transport in AFIs is typically investigated via transport measurements in a nonlocal geometry, in which two patterned heavy metal strips with a large spin-orbit coupling serve as a spin injector and detector via the spin Hall effect and inverse spin Hall effect, respectively. The AFI embedded between the two metallic contacts provides the spin transport channel (*15*, *16*, *18*, *19*). The characteristic spin diffusion length is obtained by measuring the spatially dependent variation of the longitudinal (relative to the magnetic order) spin accumulation. An essential element in the nonlocal measurement scheme is an external spin bias established by either electrical spin Hall injection or temperature gradient (*20*–*22*), which is usually sensitive to interfacial/surface conditions and is challenging to be precisely controlled in miniaturized spintronic devices.

Here, we report a noninvasive measurement technique that takes advantage of nitrogen-vacancy (NV) centers in diamond to reveal the intrinsic spin transport properties of the archetypical AFI $\alpha$-$Fe_2O_3$ (*10*, *15*, *19*). We show explicitly that NV centers offer a novel platform to probe AF spintronics, which, despite the enormous promise and expectation, is still in its infancy because of the sparse experimental approaches available. By measuring dynamic fluctuations of the spin density along the Néel order parameter, NV centers provide an alternative way to extract the intrinsic spin diffusion constant of $\alpha$-$Fe_2O_3$ in the absence of external spin stimuli. We emphasize that the probing frequency of the NV quantum sensing platform is well below the magnon band minimum, suggesting that this approach can be extended naturally to many other high-frequency magnetic systems, such as two-dimensional magnets (*23*, *24*), spin liquids (*25*), and magnetic Weyl semimetals (*26*, *27*), whose spin transport behaviors are challenging to access by conventional magnetic resonance techniques.

## RESULTS

We first briefly review the pertinent quantum-mechanical properties of NV centers. An NV center is formed by a nitrogen atom adjacent to a carbon atom vacancy in one of the nearest neighboring sites of a diamond crystal lattice (*28*). The negatively charged NV state has an $S = 1$ electron spin and serves as a three-level qubit system. Because of their excellent quantum coherence, single-spin sensitivity, and functionality in a broad temperature range (*28*, *29*), NV centers promise to be a transformative tool in exploring magnetic and electric properties in a variety of quantum materials with unprecedented field sensitivity and nanoscale spatial resolution (*30*–*32*). In our measurements, we transferred patterned diamond nanobeams containing individually addressable NV centers on the surface of an $\alpha$-$Fe_2O_3$ crystal, as illustrated in Fig. 1A. The diamond nanobeam has the shape of an equilateral triangular prism with

[1]Center for Memory and Recording Research, University of California, San Diego, La Jolla, CA 92093, USA. [2]Department of Physics and Astronomy, University of California, Los Angeles, Los Angeles, CA 90095,, USA. [3]Department of Physics, University of California, San Diego, La Jolla, CA 92093, USA. [4]Department of Physics, The University of Texas at Austin, Austin, TX 78712, USA. [5]Department of Physics, Boston College, Chestnut Hill, MA 02467, USA. [6]Department of Physics, Colorado State University, Fort Collins, CO 80523, USA.
*Corresponding author. Email: c1du@physics.ucsd.edu

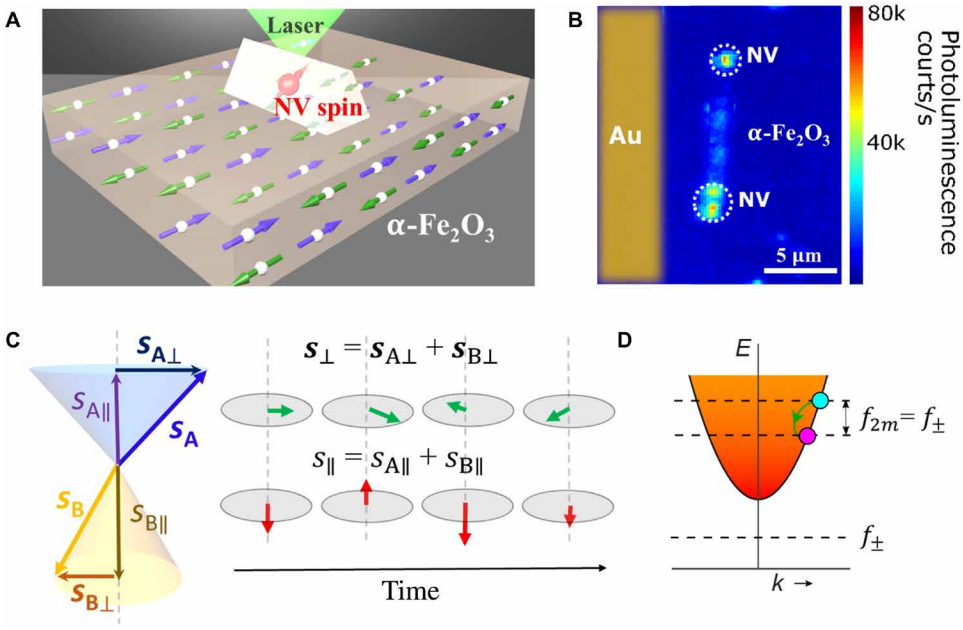


**Fig. 1. Quantum sensing of time-dependent longitudinal spin fluctuations in an antiferromagnet by NV centers.** (**A**) Schematic of a single NV spin contained in a patterned diamond nanobeam locally probing the longitudinal spin noise generated by an α-$Fe_2O_3$ crystal. (**B**) A PL image showing a diamond nanobeam containing two individually addressable NV spins positioned on top of an α-$Fe_2O_3$ crystal. (**C**) Left: Spin configuration of a Néel vector of a bipartite antiferromagnet. $\boldsymbol{s}_A$ and $\boldsymbol{s}_B$ represent the spin density of the two AF sublattices. $\boldsymbol{s}_{A\perp}$ ($\boldsymbol{s}_{B\perp}$) and $s_{A\parallel}$ ($s_{B\parallel}$) are the transverse and longitudinal components, respectively. Right: Schematic of the time-dependent fluctuations of the longitudinal and transverse spin density $s_\parallel$ and $\boldsymbol{s}_\perp$ of the Néel order. (**D**) Sketch of the magnon dispersion and the magnon density of α-$Fe_2O_3$ in the uniaxial AF phase, which falls off as 1/energy (1/*E*), as indicated by the fading colors. The full expression of the dispersion curve is given by $2\pi f_k = \sqrt{v^2k^2 + \Delta^2} \pm \Delta_B$, where $f_k$ is the frequency of a magnon at a certain wave vector *k*, v is the magnon velocity, Δ is the magnon gap, and $\Delta_B$ is the frequency gap between the two degenerate magnon modes set by the external magnetic field. In the low field regime, $\Delta_B$ is negligible compared with the AF magnon bandgap Δ. The longitudinal spin fluctuations are associated with two-magnon scattering processes, which are coupled with an NV center through dipolar interaction. $f_\pm$ corresponds to the NV electron spin resonance frequencies, and $f_{2m}$ represents the frequency of longitudinal spin fluctuations.

dimensions of 500 nm by 500 nm by 10 μm to ensure nanoscale proximity between NV centers and the sample studied (*33*–*35*). A 200-nm-thick Au stripline was fabricated on the α-$Fe_2O_3$ crystal to provide microwave control of the NV spin states (*36*). An external magnetic field *H* was applied and aligned to the NV axis. A photoluminescence (PL) image shows two individual NV centers positioned on top of the α-$Fe_2O_3$ crystal (Fig. 1B), demonstrating the single-spin addressability of the measurement platform.

α-$Fe_2O_3$ exhibits a characteristic Morin phase transition at a critical temperature ($T_M$) of ~263 K, where it changes from an easy-plane, canted AFI to a conventional uniaxial AFI with an easy axis along the [0001] crystalline orientation (*15*, *17*). We first focus on the uniaxial AF state with a temperature below $T_M$. Figure 1C illustrates the time-dependent fluctuations of the transverse and longitudinal spin density $\boldsymbol{s}_\perp$ and $s_\parallel$ of the Néel vector of α-$Fe_2O_3$ at thermal equilibrium. The dynamical opening angle of the two sublattices is exaggerated for clarity. The local fluctuations of $\boldsymbol{s}_\perp(t)$ and $s_\parallel(t)$ generate the magnetic noise $\delta\mathbf{B}_\perp(t)$ and $\delta\mathbf{B}_\parallel(t)$, respectively. Such magnetic noise can be understood by invoking the Holstein-Primakoff transformation: $\boldsymbol{s}_\perp \propto \alpha^+(\alpha)$, $s_\parallel \propto s - \alpha^+\alpha$, with $\alpha^+(\alpha)$ being the magnon creation (annihilation) operator (*37*). In an intuitive picture, the transverse spin noise $\delta\mathbf{B}_\perp(t)$ is related to one-magnon scattering processes (*34*, *38*, *39*), i.e., the creation or annihilation of magnons, which vanish at frequencies below the magnon band minimum. The longitudinal spin noise $\delta\mathbf{B}_\parallel(t)$ is related to two-magnon scattering processes, where a magnon with frequency $f + f_{2m}$ can undergo a transition to another magnon with frequency *f* (or vice versa), emitting magnetic noise at frequency $f_{2m}$ as illustrated in Fig. 1D (*38*, *39*). Microscopically, the time-dependent fluctuations of the longitudinal spin density $s_\parallel$ reflect spin transport via Brownian motion and naturally connect to the intrinsic spin diffusion constant *D* through the conventional diffusion equation (in the absence of an external magnetic field) (*38*, *40*)

$$\partial_t s_\parallel - D\nabla^2 s_\parallel = -\frac{1}{\tau_s} s_\parallel \quad (1)$$

where $\tau_s$ is the coarse-grained spin relaxation time. Figure 1D illustrates the magnon band structure of α-$Fe_2O_3$ in the uniaxial AF phase and the generation of longitudinal spin noise. In contrast to the transverse counterpart with a minimum frequency determined by the magnon bandgap, the frequency of the longitudinal spin noise starts from zero and extends to the available magnon band energy (*38*), which can be addressed by NV centers in the low gigahertz frequency regime.

We used NV relaxometry measurements (*28*, *34*, *41*, *42*) to detect the longitudinal spin noise generated by the α-$Fe_2O_3$ crystal. Figure 2A (top) shows the optical and microwave measurement sequence. A 3-μs-long green laser pulse is first applied to initialize the NV spin to the $m_s = 0$ state. Spin fluctuations in the α-$Fe_2O_3$ crystal couple to the NV centers through dipolar interactions. Longitudinal spin noise at frequencies $f_\pm$ induces NV spin transitions from the $m_s = 0$ to the $m_s = \pm1$ states, leading to an enhancement in the NV relaxation rates $\Gamma_\pm$. Here, $f_\pm$ and $\Gamma_\pm$ correspond to the NV electron spin resonance (ESR) frequencies and NV relaxation rates

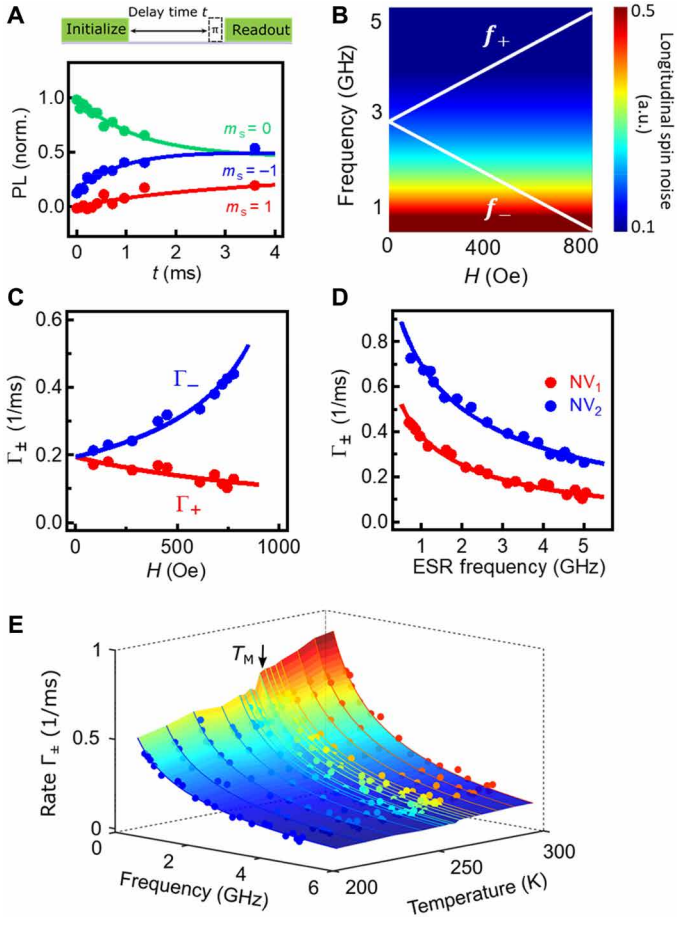


**Fig. 2. Local measurements of longitudinal spin fluctuations in α-$Fe_2O_3$ by NV relaxometry.** (**A**) Top: Optical and microwave sequence for NV relaxometry measurements. Bottom: A set of NV relaxation data measured with $H = 745$ Oe. The curves are fitted to a three-level model to extract the NV relaxation rate. (**B**) Calculated longitudinal spin noise spectrum. a.u., arbitrary units. The white curves correspond to the characteristic NV ESR frequencies $f_\pm = 2.87 \pm \tilde{\gamma}H/2\pi$. (**C**) Obtained spin relaxation rates $\Gamma_\pm$ of $NV_1$ as a function of $H$. The red and blue points correspond to $\Gamma_+$ and $\Gamma_-$, respectively. The curves are fitting to Eq. 3. (**D**) Spin relaxation rates $\Gamma_\pm$ of $NV_1$ (red dots) and $NV_2$ (blue dots) measured as a function of the NV ESR frequency, which are in agreement with the theoretical model (red and blue curves). The $NV_1$ and $NV_2$ were set at two different distances to the surface of the α-$Fe_2O_3$ crystal. (**E**) NV relaxation rates $\Gamma_\pm$ measured as a function of temperature and NV ESR frequencies, from which the temperature dependence of the diffusive constant is extracted. The solid lines are the fitting curves to the theory.

of the $m_s = 0 \longleftrightarrow \pm 1$ transitions, respectively. Compared with the $m_s = 0$ state, the optically excited $m_s = \pm 1$ states are more likely to be trapped by a dark pathway through an intersystem crossing and back to the $m_s = 0$ ground state, exhibiting a reduced PL. After delay time $t$, we measure the occupation probabilities of the NV spin at the $m_s = 0$ and the $m_s = \pm 1$ states by applying a microwave π pulse on the corresponding ESR frequencies and measuring the spin-dependent PL during the first ~600 ns of the green laser readout pulse. By measuring the integrated PL intensity as a function of the delay time $t$ and fitting the data with a three-level model (*34*), NV relaxation rates can be quantitatively obtained (see section S1 for details).

Invoking perturbation theory, the measured NV relaxation rate $\Gamma_\pm$ induced by the spin noise longitudinal to the Néel order parameter at the NV ESR frequencies $f_\pm$ can be expressed as follows (*43*)

$$\Gamma_\pm(f_\pm) = \frac{|\tilde{\gamma}\delta B_\parallel(f_\pm)|^2}{2} \quad (2)$$

where $|\delta B_\parallel(f_\pm)|^2$ is the spectral density of the longitudinal spin noise that is projected transversely to the NV orientation, and $\tilde{\gamma}$ is the gyromagnetic ratio of the NV spin. According to the fluctuation-dissipation theorem, $|\delta B_\parallel(f_\pm)|^2$ is related to the imaginary part of the longitudinal dynamic spin susceptibility $\chi''$, which can be further expressed as a function of the intrinsic spin diffusion constant $D$ via Eq. 1. In the high temperature limit appropriate for our NV measurements, $\Gamma_\pm$ can be written as (see section S2 for details) (*38*)

$$\Gamma_\pm(f_\pm) = \frac{(\gamma\tilde{\gamma})^2 k_B T}{2\pi f_\pm} \int f(\mathbf{k}, d)\chi''(D)d\mathbf{k} \quad (3)$$

where γ is the gyromagnetic ratio of the magnetic sample, $k_B$ is the Boltzmann constant, $T$ is the temperature, $\mathbf{k}$ is the wave vector of magnons, and $f(\mathbf{k}, d)$ is the transfer function describing the magnetic fields generated at the NV site (*38*, *43*). By setting the frequency to an arbitrary value in Eq. 3, we calculate the longitudinal spin noise spectrum as shown in Fig. 2B. Qualitatively, the NV relaxation rate induced by the longitudinal spin noise is higher (lower) at a lower (higher) ESR frequency, corresponding to a smaller (larger) energy difference invoked in the two-magnon process discussed above.

In our experiments, we used two NV centers ($NV_1$ and $NV_2$) with different NV-to-sample distances ($d_1 = 250 \pm 6$ nm and $d_2 = 185 \pm 5$ nm; see section S3 for details) to perform the NV relaxometry measurements. Figure 2A (bottom) shows a set of spin relaxation data measured on $NV_1$ when $H = 745$ Oe and $T = 200$ K. The measured PL intensity corresponding to the $m_s = 0$ (±1) state decreases (increases) as a function of the delay time, indicating a relaxation of the NV spin to a mixture of the $m_s = 0$ and the $m_s = \pm 1$ states. Figure 2C shows the extracted NV spin relaxation rate $\Gamma_\pm$ as a function of $H$. The measured magnetic field dependence of $\Gamma_\pm$ is in agreement with the calculated magnetic noise spectrum, as shown in Fig. 2B.

To quantitatively determine the intrinsic spin diffusion constant of the α-$Fe_2O_3$ crystal, we fit the NV ESR frequency dependence of the measured relaxation rates $\Gamma_\pm$ to Eq. 3. The agreement between the experimental results and the theoretical model, as shown in Fig. 2D, provides strong evidence that we are indeed probing the spin noise generated by the longitudinal spin fluctuation. The intrinsic spin diffusion constant $D$ of α-$Fe_2O_3$ is obtained to be $(8.9 \pm 0.5) \times 10^{-4}$ $m^2/s$ at 200 K, from which the spin conductivity is calculated to be $(6.6 \pm 0.4) \times 10^6$ S/m (see section S4 for details). We highlight that the measurements by two NV centers ($NV_1$ and $NV_2$) set at different distances to the sample surface give the same spin diffusion constant of the α-$Fe_2O_3$ crystal, which is independent of the details of the NV quantum spin sensors. Taking the measured spin diffusion constant and the magnon velocity $v \sim 30$ km/s (*44*), we get momentum scattering time of ~3 ps and a magnon mean free path of ~90 nm for α-$Fe_2O_3$. Using spin relaxation time $\tau_s = 10$ ns, which is suggested by a rough estimation in (*45*), the spin diffusion length $\lambda = \sqrt{D\tau_s}$ of α-$Fe_2O_3$ is estimated to be 3 μm at 200 K, in agreement with values reported by the nonlocal spin transport measurements

(*15*, *17*). Note that the magnon mean free path is orders of magnitude smaller than the estimated spin diffusion length, confirming the diffusive nature of AF magnons in α-$Fe_2O_3$. Figure 2E plots a three-dimensional map of the NV relaxation rates $\Gamma_{\pm}$ as a function of ESR frequency and temperature. The variation of the NV relaxation rate agrees well with the theoretical model, from which the intrinsic spin diffusion constant at individual temperatures is extracted. Note that the magnon spectrum of α-$Fe_2O_3$ is generally gapped on both sides of the Morin transition. Below the Morin transition temperature, the magnon gap is dominated by the exchange energy and the uniaxial magnetic anisotropy in the low field regime. Above the Morin transition temperature, the magnon gap is significantly reduced because of the small basal plane anisotropy of α-$Fe_2O_3$. Nevertheless, the minimal magnon energies of α-$Fe_2O_3$ in both cases are larger than the NV ESR frequencies in the magnetic field range of our study (*46*); therefore, the measured NV relaxation rates are driven by the longitudinal spin fluctuations of α-$Fe_2O_3$, and our theoretical model and analysis remain valid in the entire temperature range of study.

Recently, nonlocal spin transport behaviors have been studied in α-$Fe_2O_3$ crystals (films) in both the easy-plane and uniaxial AFI phases (*15*, *19*). Next, we investigate the temperature dependence of the intrinsic spin diffusion constant of α-$Fe_2O_3$. In particular, we are interested in revealing the variation of spin diffusion constant across the Morin phase transition. Figure 3A shows a temperature dependence of the magnetization of the α-$Fe_2O_3$ crystal measured by vibrating sample magnetometer. The external magnetic field is set to be 1000 Oe, perpendicular to the [0001] crystalline axis. Above the Morin transition temperature ($T_M$ ~ 263 K), a weak canted magnetic moment exists in the (0001) magnetic easy plane, which is confirmed by a field-dependent magnetization curve as shown in the inset. When $T < T_M$, there is a near absence of a ferromagnetic moment. Figure 3B shows the temperature dependence of the spin diffusion constant $D$ measured between 200 and 300 K, which exhibits a gradual decrease from (8.9 ± 0.5) × $10^{-4}$ to (6.6 ± 0.4) × $10^{-4}$ $m^2/s$. Notably, $D$ smoothly varies across the Morin transition temperature. Theoretically, the intrinsic spin diffusion constant is determined by the magnon velocity $v \sim \frac{J_s a}{\hbar}$ ($J_s$ is the exchange constant, $a$ is the lattice constant, and $\hbar$ is the reduced Planck constant) (*47*) and the momentum relaxation time τ as follows: $D = \frac{v^2 \tau}{3}$ (*45*). Momentum relaxation time τ in magnetic crystals (films) is determined by disorder, phonons, and Umklapp scattering (*21*). As the temperature increases, the inelastic scattering rate also increases, leading to a reduced τ and a spin diffusion constant as shown in Fig. 3B. Above the Morin transition temperature, a small canted magnetic moment emerges in the easy-plane AF phase of α-$Fe_2O_3$. While the canted magnetic moment induces variations in the magnon band structure, we note that AF spin transport in equilibrium state is mainly driven by thermal magnons governed by the exchange interaction, and the variation of magnetic anisotropies and Dzyaloshinskii-Moriya interaction can be treated as small corrections on the thermal energy scale (*46*). This is consistent with our observation that the spin diffusion constant extracted from our NV relaxometry measurements exhibits a smooth variation across the Morin phase transition.

Last, we remark that NV relaxometry could be further used to reveal the intrinsic magnetic phase transition of α-$Fe_2O_3$. Figure 3C plots the temperature-dependent NV relaxation rate $\Gamma_-$ measured between 200 and 300 K. As discussed above, the magnetic stray field

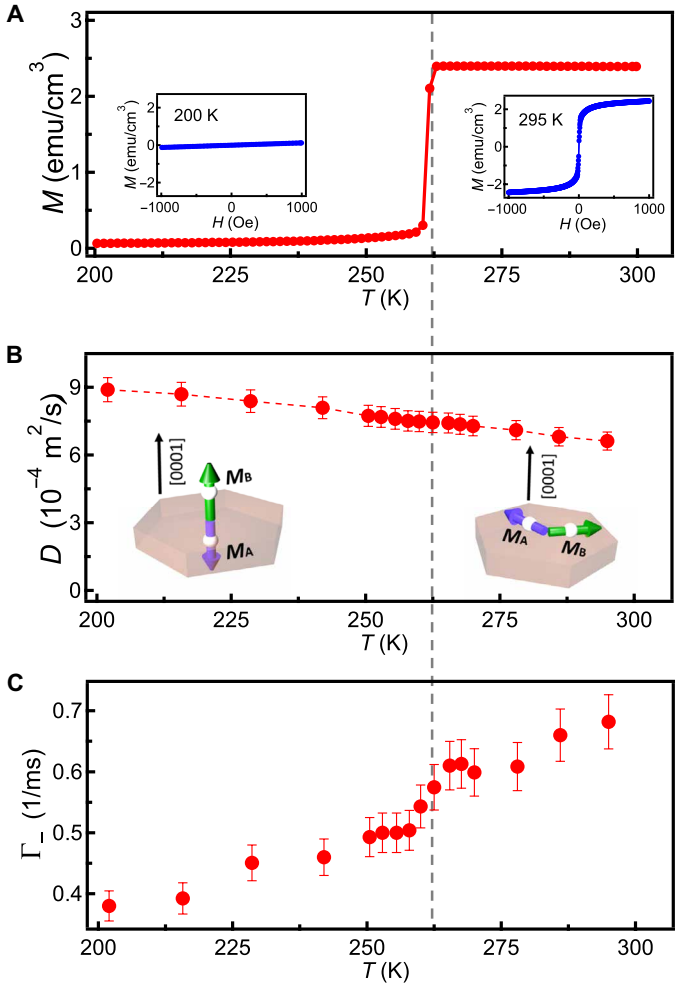


**Fig. 3. Temperature-dependent spin diffusion constant and magnetic phase transition of α-$Fe_2O_3$ probed by NV relaxometry.** (**A**) Temperature dependence of the magnetization of the α-$Fe_2O_3$ crystal with an external magnetic field of 1000 Oe applied perpendicular to the [0001] crystalline axis. Insets: Field-dependent magnetization of the α-$Fe_2O_3$ crystal when $T$ = 200 and 295 K. The dashed line represents the Morin transition temperature of α-$Fe_2O_3$. (**B**) Intrinsic spin diffusion constant $D$ measured as a function of temperature between 200 and 300 K. Insets: Schematic views of the magnetic order of α-$Fe_2O_3$ below and above the Morin transition temperature. $M_A$ and $M_B$ illustrate the magnetic moment of the two AF spin sublattices. (**C**) NV relaxation rate $\Gamma_-$ measured as a function of temperature. The external magnetic field $H$ is set to be 683 Oe, corresponding to an NV ESR frequency $f_-$ of 0.96 GHz.

$\delta\mathbf{B}_\parallel$ generated by the fluctuating longitudinal spin density of α-$Fe_2O_3$ interacts with the NV spin **S** through Zeeman coupling $\delta\mathbf{B}_\parallel \cdot \mathbf{S}$, leading to an enhancement of NV relaxation rates. The measured $\Gamma_-$ increases with increasing temperature, indicating that the magnetic noise scales with the magnon density. Across the Morin transition temperature ($T_M$ ~ 263 K), the Néel order rotates from the magnetic easy-plane to the easy-axis direction accompanied by a change of the component of the produced stray field $\delta\mathbf{B}_\parallel$ that is projected transversely to the NV axis, leading to a variation of the NV relaxation. In a macro-spin picture, the measured NV relaxation rate should follow a step-like jump in a narrow temperature window across the Morin phase transition. However, in real experiments,

magnetic domains could be formed in the α-$Fe_2O_3$ sample, especially when close to the first-order phase temperature. Note that the spatial sensitivity of our measurement technique is determined by the NV-to-sample distance, which is about 200 nm in this study. We expect that magnetic domains with dimensions comparable to (smaller than) this length scale are formed when close to the Morin transition regime, leading to a gradual variation of the measured NV relaxation rates (see the details of the numerical analysis in section S5).

## DISCUSSION

In summary, we have demonstrated NV centers as a local probe of intrinsic spin transport properties of a proximal AFI. In contrast to existing measurement platforms that involve integrating materials into the device structure, NV centers access the spin diffusion constant noninvasively by probing the local (equilibrium) longitudinal spin fluctuations in the time domain, which obviates the requirement of an external spin bias. We highlight that this merit is of particular relevance when it comes to investigating spin transport in high-frequency magnetic materials, whose coherent spin resonances are challenging to excite. In addition, the presented NV relaxometry method does not depend on the form of created NV centers in diamond, which can be naturally extended to many other NV measurement schemes. By using scanning NV microscopy or diamond nanopatterns with shallowly implanted NV centers (*31*, *32*), we expect that the spatial resolution of the presented NV quantum sensing platform could ultimately reach the nanometer scale, offering new opportunities to reveal emergent spin transport in a broad class of material systems.

## MATERIALS AND METHODS

### Sample information

The α-$Fe_2O_3$ crystal with dimensions of 0.5 mm by 5 mm by 5 mm was obtained commercially from the company SurfaceNet and was orientated with $[11\bar{2}0]$ out of the sample plane. The crystal structure and surface morphology of the α-$Fe_2O_3$ crystal have been characterized by x-ray diffraction and atomic force microscopy, as shown in fig. S1. The Morin transition temperature was characterized to be ~263 K by temperature-dependent magnetometry measurements. Above the Morin transition temperature, α-$Fe_2O_3$ behaves as an easy-plane antiferromagnet, exhibiting a weak canted magnetic moment ($M_s \sim 2$ emu/cm$^3$) in (0001) plane because of the Dzyaloshinskii-Moriya interaction. Below the Morin transition temperature, the sign of the anisotropy field along the [0001] axis changes, and α-$Fe_2O_3$ behaves as a uniaxial antiferromagnet with an easy axis along the [0001] crystalline orientation.

### Device fabrication

Diamond nanobeams were fabricated by a combination of top-down etching and angled etching processes (*33*). Acid cleaning (*48*) was performed before and after the fabrication processes to ensure a pristine diamond surface. Patterned diamond nanobeams containing individually addressable NV centers were transferred onto the surface of an α-$Fe_2O_3$ crystal using a tungsten tip performed on a micromechanical transfer stage (fig. S2A). The out-of-plane orientation of the NV axis was experimentally confirmed to be the same (within experimental errors) before and after the transfer process, excluding the possibility of rotation or tilting of diamond nanobeams. The NV orientation is obtained by magnetic field alignment. We measured the NV PL as a function of the position of the permanent magnet, and the external magnetic field aligns with the NV axis when the NV centers emit the maximum PL. The NV spin state was controlled by microwave currents flowing a 5-μm-wide and 200-nm-thick Au on-chip stripline patterned on the α-$Fe_2O_3$ crystal. The distance between the diamond nanobeam and the Au stripline is about 3 μm, ensuring a sufficiently large microwave field applied at the NV site (fig. S2B). The angle between the NV axis and the surface normal for the two NV centers ($NV_1$ and $NV_2$) positioned on top of the α-$Fe_2O_3$ crystal is 59°.

### NV measurements

NV measurements were performed in a closed-loop optical cryostat with a working temperature from 4 to 350 K. We optically addressed individual NV centers using a home-built scanning confocal microscope. A 532-nm continuous laser (Hubner Photonics) was used for optical excitation of the NV centers. Laser pulses for optical initialization and readout of NV centers were generated by an acoustic-optical modulator in a double-pass configuration. Microwave signals used for driving NV centers were generated by Rohde & Schwarz signal generators (SGS100a and SMB100A). The microwave currents were delivered to microwave switches (Mini-Circuits ZASWA-2-50DRA+), a microwave combiner (Mini-Circuits ZB3PD-63-S+), and an amplifier with +50-dB amplification (Mini-Circuits ZHL-25 W-63+) and, lastly, sent to the on-chip Au stripline via a printed circuit board. NV PL was detected by an avalanche photo diode (Excelitas SPCM-AQRH-13). The trigger pulses to the optical modulator and photon counting were generated by a programmable pulse generator (Spincore, PBESR-PRO-500). The external magnetic field was generated by a cylindrical NdFeB permanent magnet attached to a scanning stage. The magnitude and the orientation of the magnetic field can be controlled by moving the position of the permanent magnet. Extended NV relaxometry measurements are presented in section S6 to show the direct comparison between the longitudinal and transverse spin fluctuations.

## SUPPLEMENTARY MATERIALS

Supplementary material for this article is available at https://science.org/doi/10.1126/sciadv.abg8562

## REFERENCES AND NOTES


1. V. Baltz, A. Manchon, M. Tsoi, T. Moriyama, T. Ono, Y. Tserkovnyak, Antiferromagnetic spintronics. *Rev. Mod. Phys.* **90**, 015005 (2018).
2. T. Jungwirth, J. Sinova, A. Manchon, X. Marti, J. Wunderlich, C. Felser, The multiple directions of antiferromagnetic spintronics. *Nat. Phys.* **14**, 200–203 (2018).
3. S. M. Rezende, A. Azevedo, R. L. Rodríguez-Suárez, Introduction to antiferromagnetic magnons. *J. Appl. Phys.* **126**, 151101 (2019).
4. J. Li, C. B. Wilson, R. Cheng, M. Lohmann, M. Kavand, W. Yuan, M. Aldosary, N. Agladze, P. Wei, M. S. Sherwin, J. Shi, Spin current from sub-terahertz-generated antiferromagnetic magnons. *Nature* **578**, 70–74 (2020).
5. P. Vaidya, S. A. Morley, J. van Tol, Y. Liu, R. Cheng, A. Brataas, D. Lederman, E. del Barco, Subterahertz spin pumping from an insulating antiferromagnet. *Science* **368**, 160–165 (2020).
6. S. M. Wu, W. Zhang, A. Kc, P. Borisov, J. E. Pearson, J. S. Jiang, D. Lederman, A. Hoffmann, A. Bhattacharya, Antiferromagnetic spin Seebeck effect. *Phys. Rev. Lett.* **116**, 097204 (2016).
7. W. Zhang, M. B. Jungfleisch, W. Jiang, J. E. Pearson, A. Hoffmann, F. Freimuth, Y. Mokrousov, Spin Hall effects in metallic antiferromagnets. *Phys. Rev. Lett.* **113**, 196602 (2014).
8. T. Kosub, M. Kopte, R. Hühne, P. Appel, B. Shields, P. Maletinsky, R. Hübner, M. O. Liedke, J. Fassbender, O. G. Schmidt, D. Makarov, Purely antiferromagnetic magnetoelectric random access memory. *Nat. Commun.* **8**, 13985 (2017).

9. P. Wadley, B. Howells, J. Železný, C. Andrews, V. Hills, R. P. Campion, V. Novák, K. Olejník, F. Maccherozzi, S. S. Dhesi, S. Y. Martin, T. Wagner, J. Wunderlich, F. Freimuth, Y. Mokrousov, J. Kuneš, J. S. Chauhan, M. J. Grzybowski, A. W. Rushforth, K. Edmond, B. L. Gallagher, T. Jungwirth, Electrical switching of an antiferromagnet. *Science* **351**, 587–590 (2016).
10. Y. Cheng, S. Yu, M. Zhu, J. Hwang, F. F. Yang, Electrical switching of tristate antiferromagnetic Néel order in $\alpha$-$Fe_2O_3$ epitaxial films. *Phys. Rev. Lett.* **124**, 027202 (2020).
11. X. Z. Chen, R. Zarzuela, J. Zhang, C. Song, X. F. Zhou, G. Y. Shi, F. Li, H. A. Zhou, W. J. Jiang, F. Pan, Y. Tserkovnyak, Antidamping-torque-induced switching in biaxial antiferromagnetic insulators. *Phys. Rev. Lett.* **120**, 207204 (2018).
12. M. S. Wörnle, P. Welter, Z. Kašpar, K. Olejník, V. Novák, R. P. Campion, P. Wadley, T. Jungwirth, C. L. Degen, P. Gambardella, Current-induced fragmentation of antiferromagnetic domains (2019);http://arxiv.org/abs/1912.05287.
13. I. Gray, T. Moriyama, N. Sivadas, G. M. Stiehl, J. T. Heron, R. Need, B. J. Kirby, D. H. Low, K. C. Nowack, D. G. Schlom, D. C. Ralph, T. Ono, G. D. Fuchs, Spin Seebeck imaging of spin-torque switching in antiferromagnetic Pt/NiO heterostructures. *Phys. Rev. X* **9**, 041016 (2019).
14. C. C. Chiang, S. Y. Huang, D. Qu, D. P. H. Wu, C. L. Chien, Absence of evidence of electrical switching of the antiferromagnetic Néel vector. *Phys. Rev. Lett.* **123**, 227203 (2019).
15. R. Lebrun, A. Ross, S. A. Bender, A. Qaiumzadeh, L. Baldrati, J. Cramer, A. Brataas, R. A. Duine, M. Kläui, Tunable long-distance spin transport in a crystalline antiferromagnetic iron oxide. *Nature* **561**, 222–225 (2018).
16. W. Yuan, Q. Zhu, T. Su, Y. Yao, W. Xing, Y. Chen, Y. Ma, X. Lin, J. Shi, R. Shindou, X. C. Xie, W. Han, Experimental signatures of spin superfluid ground state in canted antiferromagnet $Cr_2O_3$ via nonlocal spin transport. *Sci. Adv.* **4**, eaat1098 (2018).
17. R. Lebrun, A. Ross, O. Gomonay, V. Baltz, U. Ebels, A. L. Barra, A. Qaiumzadeh, A. Brataas, J. Sinova, M. Kläui, Long-distance spin-transport across the Morin phase transition up to room temperature in the ultra-low damping single crystals of the antiferromagnet $\alpha$-$Fe_2O_3$. *Nat. Commun.* **11**, 6332 (2020).
18. T. Wimmer, A. Kamra, J. Gückelhorn, M. Opel, S. Geprägs, R. Gross, H. Huebl, M. Althammer, Observation of antiferromagnetic magnon pseudospin dynamics and the Hanle effect. *Phys. Rev. Lett.* **125**, 247204 (2020).
19. J. Han, P. Zhang, Z. Bi, Y. Fan, T. S. Safi, J. Xiang, J. Finley, L. Fu, R. Cheng, L. Liu, Birefringence-like spin transport via linearly polarized antiferromagnetic magnons. *Nat. Nanotechnol.* **15**, 563–568 (2020).
20. L. J. Cornelissen, J. Liu, R. A. Duine, J. Ben Youssef, B. J. van Wees, Long-distance transport of magnon spin information in a magnetic insulator at room temperature. *Nat. Phys.* **11**, 1022–1026 (2015).
21. L. J. Cornelissen, K. J. H. Peters, G. E. W. Bauer, R. A. Duine, B. J. van Wees, Magnon spin transport driven by the magnon chemical potential in a magnetic insulator. *Phys. Rev. B* **94**, 014412 (2016).
22. B. L. Giles, Z. Yang, J. S. Jamison, R. C. Myers, Long-range pure magnon spin diffusion observed in a nonlocal spin-Seebeck geometry. *Phys. Rev. B* **92**, 224415 (2015).
23. K. S. Burch, D. Mandrus, J.-G. Park, Magnetism in two-dimensional van der Waals materials. *Nature* **563**, 47–52 (2018).
24. W. Wang, M. W. Daniels, Z. Liao, Y. Zhao, J. Wang, G. Koster, G. Rijnders, C.-Z. Chang, D. Xiao, W. Wu, Spin chirality fluctuation in two-dimensional ferromagnets with perpendicular magnetic anisotropy. *Nat. Mater.* **18**, 1054–1059 (2019).
25. L. Savary, L. Balents, Quantum spin liquids: A review. *Rep. Prog. Phys.* **80**, 016502 (2017).
26. S. Nakatsuji, N. Kiyohara, T. Higo, Large anomalous Hall effect in a non-collinear antiferromagnet at room temperature. *Nature* **527**, 212–215 (2015).
27. S. Zhang, Y. Tserkovnyak, Flavors of noise in magnetic Weyl semimetals (2021); https://arxiv.org/abs/2108.07305.
28. L. Rondin, J.-P. Tetienne, T. Hingant, J.-F. Roch, P. Maletinsky, V. Jacques, Magnetometry with nitrogen-vacancy defects in diamond. *Reports Prog. Phys.* **77**, 056503 (2014).
29. G. Q. Liu, X. Feng, N. Wang, Q. Li, R. B. Liu, Coherent quantum control of nitrogen-vacancy center spins near 1000 kelvin. *Nat. Commun.* **10**, 1344 (2019).
30. A. Laraoui, H. Aycock-Rizzo, Y. Gao, X. Lu, E. Riedo, C. A. Meriles, Imaging thermal conductivity with nanoscale resolution using a scanning spin probe. *Nat. Commun.* **6**, 8954 (2015).
31. M. Pelliccione, A. Jenkins, P. Ovartchaiyapong, C. Reetz, E. Emmanouilidou, N. Ni, A. C. Bleszynski Jayich, Scanned probe imaging of nanoscale magnetism at cryogenic temperatures with a single-spin quantum sensor. *Nat. Nanotechnol.* **11**, 700–705 (2016).
32. L. Thiel, Z. Wang, M. A. Tschudin, D. Rohner, I. Gutiérrez-Lezama, N. Ubrig, M. Gibertini, E. Giannini, A. F. Morpurgo, P. Maletinsky, Probing magnetism in 2D materials at the nanoscale with single-spin microscopy. *Science* **364**, 973–976 (2019).
33. M. J. Burek, N. P. de Leon, B. J. Shields, B. J. M. Hausmann, Y. Chu, Q. Quan, A. S. Zibrov, H. Park, M. D. Lukin, M. Lončar, Free-standing mechanical and photonic nanostructures in single-crystal diamond. *Nano Lett.* **12**, 6084–6089 (2012).
34. C. H. R. Du, T. Van der Sar, T. X. Zhou, P. Upadhyaya, F. Casola, H. Zhang, M. C. Onbasli, C. A. Ross, R. L. Walsworth, Y. Tserkovnyak, A. Yacoby, Control and local measurement of the spin chemical potential in a magnetic insulator. *Science* **357**, 195–198 (2017).
35. E. Lee-Wong, R. L. Xue, F. Y. Ye, A. Kreisel, T. van der Sar, A. Yacoby, C. H. R. Du, Nanoscale detection of magnon excitations with variable wavevectors through a quantum spin sensor. *Nano Lett.* **20**, 3284–3290 (2020).
36. G. D. Fuchs, V. V. Dobrovitski, D. M. Toyli, F. J. Heremans, D. D. Awschalom, Gigahertz dynamics of a strongly driven single quantum spin. *Science* **326**, 1520–1522 (2009).
37. T. Holstein, H. Primakoff, Field dependence of the intrinsic domain magnetization of a ferromagnet. *Phys. Rev.* **58**, 1098–1113 (1940).
38. B. Flebus, Y. Tserkovnyak, Quantum-impurity relaxometry of magnetization dynamics. *Phys. Rev. Lett.* **121**, 187204 (2018).
39. B. A. McCullian, A. M. Thabt, B. A. Gray, A. L. Melendez, M. S. Wolf, V. L. Safonov, D. V. Pelekhov, V. P. Bhallamudi, M. R. Page, P. C. Hammel, Broadband multi-magnon relaxometry using a quantum spin sensor for high frequency ferromagnetic dynamics sensing. *Nat. Commun.* **11**, 5229 (2020).
40. S. S. L. Zhang, S. Zhang, Magnon mediated electric current drag across a ferromagnetic insulator layer. *Phys. Rev. Lett.* **109**, 096603 (2012).
41. M. R. Page, F. Guo, C. M. Purser, J. G. Schulze, T. M. Nakatani, C. S. Wolfe, J. R. Childress, P. C. Hammel, G. D. Fuchs, V. P. Bhallamudi, Optically detected ferromagnetic resonance in diverse ferromagnets via nitrogen vacancy centers in diamond. *J. Appl. Phys.* **126**, 124902 (2019).
42. J. P. Tetienne, T. Hingant, L. Rondin, A. Cavaillès, L. Mayer, G. Dantelle, T. Gacoin, J. Wrachtrup, J. F. Roch, V. Jacques, Spin relaxometry of single nitrogen-vacancy defects in diamond nanocrystals for magnetic noise sensing. *Phys. Rev. B* **87**, 235436 (2013).
43. T. van der Sar, F. Casola, R. Walsworth, A. Yacoby, Nanometre-scale probing of spin waves using single-electron spins. *Nat. Commun.* **6**, 7886 (2015).
44. E. J. Samuelsen, G. Shirane, Inelastic neutron scattering investigation of spin waves and magnetic interactions in $\alpha$-$Fe_2O_3$. *Phys. Status Solidi B* **42**, 241–256 (1970).
45. K. Shen, Magnon spin relaxation and spin Hall effect due to the dipolar interaction in antiferromagnetic insulators. *Phys. Rev. Lett.* **124**, 077201 (2020).
46. P. R. Elliston, G. J. Troup, Some antiferromagnetic resonance measurements in $\alpha$-$Fe_2O_3$. *J. Phys. C* **1**, 169–178 (1968).
47. S. Chatterjee, J. F. Rodriguez-Nieva, E. Demler, Diagnosing phases of magnetic insulators via noise magnetometry with spin qubits. *Phys. Rev. B* **99**, 104425 (2019).
48. D. B. Bucher, D. P. L. Aude Craik, M. P. Backlund, M. J. Turner, O. Ben Dor, D. R. Glenn, R. L. Walsworth, Quantum diamond spectrometer for nanoscale NMR and ESR spectroscopy. *Nat. Protoc.* **14**, 2707–2747 (2019).
49. K. Y. Guslienko, A. N. Slavin, Magnetostatic Green's functions for the description of spin waves in finite rectangular magnetic dots and stripes. *J. Magn. Magn. Mater.* **323**, 2418–2424 (2011).
50. A. Rustagi, I. Bertelli, T. van der Sar, P. Upadhyaya, Sensing chiral magnetic noise via quantum impurity relaxometry. *Phys. Rev. B* **102**, 220403(R) (2020).
51. B. Flebus, Chemical potential of an antiferromagnetic magnon gas. *Phys. Rev. B* **100**, 064410 (2019).


**Acknowledgments:** We would like to thank F. Casola for fabricating the diamond nanobeams. **Funding:** N.J.M. and C.R.D. were supported by Air Force Office of Scientific Research under award FA9550-20-1-0319 and its Young Investigator Program under award FA9550-21-1-0125. M.H. and C.R.D. acknowledge the support from U.S. NSF under award DMR-2046227 and ECCS-2029558. H.W., Y.X., and E.E.F. were supported by the Quantum Materials for Energy Efficient Neuromorphic Computing, an Energy Frontier Research Center funded by the U.S. Department of Energy (DOE), Office of Science, Basic Energy Sciences under award DE-SC0019273. S.Z. and Y.T. were supported by NSF under grant no. DMR-1742928. C.L. and M.W. were supported by the U.S. NSF under grants nos. EFMA-1641989 and ECCS-1915849. **Author contributions:** H.W. performed the measurements and analyzed the data with help from N.J.M. and M.H. S.Z., B.F., and Y.T. provided theoretical guidance and support. Y.X. and E.E.F. provided sample/device fabrication and characterization. C.L. and M.W. provided yttrium iron garnet thin films. C.R.D. supervised this project. **Competing interests:** The authors declare that they have no competing interests. **Data and materials availability:** All data needed to evaluate the conclusions in the paper are present in the paper and/or the Supplementary Materials.

Submitted 2 February 2021
Accepted 15 November 2021
Published 7 January 2022
10.1126/sciadv.abg8562